Distinct phenotypic consequences of cholangiocarcinoma-associated FGFR2 alterations depend on biliary epithelial maturity

O'Loughlin E[*], Zhang Y[*], Chiasson-MacKenzie C[*], Dave P, Rheinbay E, Stott S, McClatchey AI[**]

MGH Krantz Family Center for Cancer Research, Charlestown, MA 02129

Harvard Medical School, Boston MA 02112

*Equal contribution

**Correspondence: amcclatchey@mgh.harvard.edu

Abstract

Epithelial cancers disrupt tissue architecture and are often driven by mutations in genes that normally play important roles in epithelial morphogenesis. The intrahepatic biliary system is an epithelial tubular network that forms within the developing liver via the *de novo* initiation and expansion of apical lumens. Intrahepatic biliary tumors are often driven by different types of mutations in the FGFR2 receptor tyrosine kinase which plays important roles in epithelial morphogenesis in other developmental settings. Using a physiologic and quantitative 3D model we have found that FGFR signaling is important for biliary morphogenesis and that oncogenic FGFR2 mutants disrupt biliary architecture. Importantly, we found that both the trafficking and signaling of normal FGFR2 and the phenotypic consequences of FGFR2 mutants are influenced by the epithelial state of the cell. Unexpectedly, we found that different tumor-driving FGFR2 mutants disrupt biliary morphogenesis in completely different and clinically relevant ways, informing our understanding of morphogenesis and tumorigenesis and highlighting the importance of convergent studies of both.

Introduction

The acquisition of epithelial polarity and architecture is a cellular program that governs the morphogenesis of many organs, and abnormalities in epithelial tissue architecture are the first signs of cancer pathology triggered by somatic genetic mutations[1-4]. Despite the clear relationship between morphogenesis and tumorigenesis, tumor-causing mutations are usually studied in cells cultured under conditions that do not recapitulate epithelial architecture with changes in cell number used as the sole readout of activity. Oncogenic mutations in receptor tyrosine kinases (RTKs) are common tumor drivers that are assumed to enable broad and constitutive signaling and unscheduled cell division[5]. However, RTK activity also governs and is modulated by programs of epithelial polarization and maturation[6]. In addition, germline activating mutations in some RTKs cause specific developmental syndromes without increased cancer predisposition, while different cancer types exhibit strong biases in which RTKs are mutated and which type of RTK mutations are prevalent, indicating important biological RTK:tumor relationships that are not well understood[7]. Understanding these relationships will require convergent studies of morphogenesis and tumorigenesis.

Intrahepatic bile ducts (IHBDs) form a tubular tree within the liver that is essential for liver function[8]. Biliary morphogenesis occurs in an 'inside-out' manner, driven by the *de novo* formation, extension and interconnection of apical lumens within E-cadherin-positive cell-cell junctions, and is accompanied by the conversion of immature hepatoblasts to a biliary fate[9,10]. This fundamental self-organizing mechanism of epithelial polarization provides spatial control of both secretory and receptor activity in other developmental settings[11-13]. Bile duct morphogenesis is thus driven by the acquisition of epithelial polarity and architecture, but little is known about how this program is initiated or coordinated among cells to establish a biliary tree.

Congenital or acquired diseases that are associated with abnormal architecture of the intrahepatic biliary epithelial tree are fatal, including intrahepatic cholangiocarcinoma (ICC)[14,15]. Among frequent genetic drivers of ICC are several different types of mutations in the fibroblast growth factor receptor 2 (FGFR2), triggering clinical trials of pharmacologic FGFR inhibitors that have yielded modest, transient and variable success[16-19]. Importantly, FGFR signaling has also been shown to be crucial for the acquisition of epithelial architecture and specifically for *de novo* lumen formation in other developmental settings[12,13,20,21]. However, neither the biological function of FGFR in biliary morphogenesis or the proximal consequences of its unscheduled activation in biliary tumorigenesis are known.

Much has been learned about biliary morphogenesis through careful staging of the process in the developing liver[8,9,22,23]. However, *de novo* lumen formation and expansion occurs within a matter of hours and non-uniformly across the fetal liver, precluding the capture of a high-resolution or quantitative understanding of biliary morphogenesis *in vivo*. Mouse models of FGFR-driven ICC have proven difficult to generate and other ICC models feature tumors that develop after relatively long durations and with unpredictable timing and anatomical distribution, also precluding a high-resolution understanding of how they initiate[24,25]. Three dimensional (3D) organoids are widely used to model some aspects of epithelial biology, but biliary organoids established from normal or tumor tissue are large spherical cysts that neither form similarly to or recapitulate biliary architecture[26-29]. To study biliary morphogenesis and the impact of normal and oncogenic FGFR on that process at high resolution, we adapted a physiological 3D model for quantitative imaging and deployed it to analyze a panel of hepatoblast cell lines that uniquely capture discrete stages of *de novo* lumen formation and expansion. We discovered that FGFR signaling is important for normal biliary morphogenesis and that oncogenic versions of FGFR2 disrupt the process; however, we found that the signaling and cellular phenotypes triggered by oncogenic FGFR2 depend on the epithelial maturation of the cells. Surprisingly, we also found

that the morphogenetic consequences of different oncogenic FGFR2 mutants are completely distinct, and largely proliferation independent and driven by nonclassical FGFR2 signaling, which has important therapeutic implications. This work illustrates how morphogenesis can inform our understanding of tumor biology and of how tumor-driving mutants can be important tools for studying morphogenesis.

Results

Hepatoblast panel captures stages of de novo *lumen competence*

To dissect the process of *de novo* lumen formation and extension, we established a panel of clonal hepatoblast (HB) cell lines from E14.5 mouse embryos and assessed their ability to form and extend lumens in a modified 3D collagen sandwich assay (Fig. 1A; Supplemental Fig. 1A,B)[30]. Although all express the biliary markers *Hnf1b* and *Sox9*, our HB lines reproducibly exhibit one of three levels of lumen competence, representative examples of which are shown in Fig. 1A: HB[A], lumen incompetent; HB[B], immature lumen competent (many small lumens); and HB[C], mature lumen competent (large interconnecting lumens and sometimes tubular structures; Supplemental Figure 1A,B). For comparison, we deployed NIH3T3 fibroblasts that do not form lumens and Caco2 cells, mature colonic epithelial cells that form lumen-containing cystic spheres (Supplemental Fig. 1C). As they do *in vivo*, *de novo* lumens established by HB cells in 3D formed within E-cadherin-positive cell-cell junctions and were marked by a concentrated rim of actin and ERM proteins devoid of E-cadherin (Fig. 1B)[9]. We developed a quantitative fluorescence imaging workflow in which scanning of the entire 3D culture captures thousands of lumens across the equivalent of ~120 individual 20X fields of view and HALO[TM] software-based image segmentation analysis enables measurement of multiple parameters, including lumen number, size and shape (Fig. 1C). We noted that cell division decreased with lumen competence, and that lumen extension was enhanced at the 3D chamber periphery, likely due

to mechanical forces; therefore, we took lumen measurements in the peripheral half of each chamber and at equivalent cell density (Supplemental Fig. 1D-F). Together, our HB cell panel and quantitative 3D model uniquely captures discrete stages of this pivotal proliferation-independent morphogenetic process.

Lumen competence coincides with junctional maturation and apical gene expression

Our HB cell lines expressed similar levels of N-cadherin (*Cdh2*) and E-cadherin (*Cdh1*) protein and mRNA, and there was no clear transcriptional mesenchymal-to-epithelial (MET) transition accompanying the acquisition of lumen competence (Fig. 2A; Supplemental Fig. 2). However, close inspection of cell-cell junctions revealed clear evidence of junctional maturation (Fig. 2B,C). Immature lumen competence was accompanied by a striking transition from punctate perijunctional to concentrated junctional E-cadherin and a reduction in junctional N-cadherin, while mature lumen-competent cells exhibited a striking increase in junction height, loss of junctional N-cadherin, and the appearance of the tight junction component ZO-1 without an increase in *ZO-1/Tjp1* mRNA (Fig. 2B-D; Supplemental Fig. 2).

To understand how HBs acquire lumen competence we examined gene expression changes across our cell panel by bulk RNAseq (Fig. 3A). We found that the acquisition of lumen competence in HB^B and HB^C cells was associated with a striking increase in the expression of apical membrane components, including apical transporters and apical junctional components (Fig. 3B; Supplemental Fig. 3). Validation of a subset of these revealed a clear progressive increase in expression with lumen initiation and maturation (Fig. 3C). On the other hand, comparison of apical genes upregulated from HB^A→HB^B cells with those upregulated from HB^B→HB^C cells also revealed stage-specific subsets linked to lumen initiation versus maturation (Fig. 3D,E; Supplemental Fig. 3A). Notably, genes linked to bile acid metabolism were

upregulated in association with lumen initiation (HB^A→HB^B) and apical junctional components, including tight junction components, were upregulated in association with lumen maturation, consistent with our observations of junctional maturation (HB^B→HB^C transition; Fig. 3D,E; Fig. 2B). Comparison of a second mature lumen competent (HB^{Cb}) cell line with HB^B cells revealed similar upregulation of apical genes associated with lumen maturation (Supplemental Fig. 1, 3).

FGFR signaling promotes de novo lumen formation and biliary morphogenesis

In other examples of *de novo* lumen formation in development, FGFR signaling plays an important role by promoting epithelial character in a manner that is spatially restricted by the *de novo* lumens themselves[12,13]. To determine whether FGFR activity is required for *de novo* lumen formation during biliary morphogenesis, we treated 3D cultures of lumen competent HB^B cells with the clinically active FGFR kinase inhibitor (FGFRi) infigratinib. We found that FGFRi treatment of HB^B cells significantly decreased lumen number (Fig. 4A,B). Moreover, FGFRi treatment reduced the expression of apical genes associated with the acquisition of lumen competence (Fig. 4C). On the other hand, increasing FGFR signaling via exogenous expression of FGFR2^{wt} increased the expression of the same apical genes (Fig. 4D). Notably, FGFR2^{wt} also increased the expression of genes associated with basal membrane building, as also occurred during the lumen initiation phase (HB^A→HB^B; Supplemental Fig. 3A). These data support the notion that FGFR signaling promotes *de novo* lumen formation and enhances polarity and epithelial character during biliary morphogenesis as in other developmental settings.

Distinct localization and phenotypic consequences of ICC-causing FGFR2 mutants

Oncogenic *FGFR* mutations are important drivers of ICC but their cell biological impacts are not understood[31]. Most common are fusions in which the C-terminal portion of FGFR2 is replaced by a variety of partners that are thought to facilitate ligand-independent receptor dimerization;

mutations or small in-frame deletions in the extracellular domain (FGFR2^{EID}) also occur and are likewise thought to render the receptor ligand-independent (Fig. 5A)[17]. To determine whether ICC-causing FGFR alterations perturb biliary epithelial architecture, we examined the impact of expressing an FGFR2^{fusion} (FGFR2-PHGDH) or FGFR2^{EID} (FGFR2$^{WI290>C}$) in HB^{B} cells. Neither mutant had a strong effect on proliferation, but the two FGFR2 mutants yielded completely different phenotypic consequences in our physiological 3D model (Fig. 5B-E; Supplemental Fig. 5A). The FGFR2^{EID} yielded a modest increase in *de novo* lumen number but not size while the FGFR2^{fusion} completely ablated *de novo* lumen formation (Fig. 5B,C; Supplemental Fig. 5B). Close inspection revealed that the FGFR2^{fusion} but not the FGFR2^{EID}, markedly altered E-cadherin cell junctions in which *de novo* lumens form; instead of forming a discrete linear boundary between cells as in control and FGFR2^{wt}-expressing cells, E-cadherin exhibited a punctate vesicular distribution around cell-cell boundaries in FGFR2^{fusion}-expressing cells (Fig. 5C,D). The FGFR2^{fusion} if anything *increased Sox9* expression, suggesting that it does not trigger biliary dedifferentiation (Supplemental Fig. 5C). Importantly, both junctional E-cadherin integrity and lumen formation in FGFR2^{fusion}-expressing cells were rescued by FGFRi treatment (Fig. 5B-E). The differential consequences of the two mutants were further underscored by the distinct changes in gene expression they elicited; the FGFR2^{EID} increased the expression of genes that were nearly all also induced by FGFR2^{wt}, while the FGFR2^{fusion} induced a largely non-overlapping set of genes (Fig. 5F; Supplemental Fig. 5D).

The dramatically different impacts of the FGFR2^{fusion} and FGFR2^{EID} on *de novo* lumen formation in 3D could be explained by their subcellular distributions. Immunoblotting revealed that in HB^{B} cells the majority of FGFR2^{wt} is fully glycosylated but ~30% remains in an immature state of glycosylation that is uniquely sensitive to EndoH treatment (Fig. 5G). In contrast, nearly all of the FGFR2^{EID} (~98%) is in an immature state of glycosylation and trapped within the ER-Golgi in HB^{B} cells, as has been described in NIH3T3 cells (Fig. 5G; Supplemental Fig. 5D)[32]. On the

other hand, the FGFR2^{fusion} is fully glycosylated with little detectable EndoH-sensitive receptor population (Fig. 5G). Immunofluorescence revealed that the FGFR2^{fusion} is concentrated at and the FGFR2^{EID} largely excluded from cell-cell boundaries (Supplemental Fig. 5E). Surface biotinylation confirmed the enrichment of surface-available FGFR2^{fusion}, while surface-available FGFR2^{EID} was undetectable (Fig. 5H). Thus, in immature lumen-forming HB^B cells, two ICC-causing FGFR2 mutants are trafficked differently and elicit distinct phenotypic consequences.

Glycosylation and surface availability of FGFR2^{EID} depend on biliary epithelial maturation

Our HB cells exhibit a range of epithelial character, so we asked whether FGFR2^{EID} glycosylation varied across this biliary-relevant panel. We found that as in NIH3T3 and HB^B cells the FGFR2^{EID} is immaturely glycosylated and ER-Golgi-trapped in lumen-incompetent HB^A cells (Fig. 6A). However, in mature lumen-competent HB^C cells, a significant proportion of the FGFR2^{EID} is glycosylated (26%) and reaches the surface while in even more mature Caco2 epithelial cells the FGFR2^{EID} is fully glycosylated (Fig. 6A,B). Notably, the FGFR2^{EID} exhibited only an immature glycosylated form in murine AML12 hepatocytes (Supplemental Fig. 6A). Finally, we found that a second FGFR2^{EID} (FGFR2$^{H167\_N173}$) was similarly entirely immaturely glycosylated in NIH3T3 and HB^B cells but maturely glycosylated in Caco2 cells (Supplemental Fig. 6B). Therefore, the trafficking of ICC-causing FGFR2^{EID} mutants depends on epithelial character.

Junctional disruption triggered by FGFR2^{fusion} depends on biliary epithelial maturation

In contrast to the FGFR2^{EID}, the FGFR2^{fusion} was maturely glycosylated and enriched at the cell surface regardless of epithelial maturation (Fig. 5G,H, 6B). However, given the striking loss of E-cadherin junctional integrity triggered by the FGFR2^{fusion} in HB^B cells (Fig. 5D,E), and clear differences in junctional maturation exhibited across our cell panel, we asked whether the

FGFR2^{fusion} differentially impacted cell junctions according to epithelial maturity. We found that despite enhanced surface localization in all HB cells, the FGFR2^{fusion} specifically disrupted established E-cadherin-based cell junctions. In HB^B cells, the FGFR2^{fusion} disrupted the junctional distribution of E-cadherin with minimal impact on N-cadherin or F-actin (Fig. 7A-E, 5D,E). In mature lumen-competent HB^C cells, the FGFR2^{fusion} also specifically disrupted E-cadherin based junctions, but instead of the punctate junctional appearance of E-cadherin in FGFR2^{fusion}-expressing HB^B cells E-cadherin formed strong perijunctional aggregates, often at tricellular junctions (Fig. 7A-C). The FGFR2^{fusion} had no discernable effect in lumen-incompetent HB^A cells, where E-cadherin based junctions are not yet well-formed (Fig. 7A,B). In contrast, the FGFR2^{EID} had no major impact on cell junctions in HB^B or HB^C cells (Fig. 5D,E; Supplemental Fig. 7A).

Distinct phenotypic consequences of the FGFR2^{EID} and FGFR2^{fusion} on coordinated de novo *lumen formation*

Given that in mature lumen competent HB^C cells FGFR2^{EID} and FGFR2^{fusion} can both be maturely glycosylated but differentially influence cell-cell junctions (Fig. 6, 7; Supplemental Fig. 7A), we compared their impact on *de novo* lumen formation and morphogenesis in 3D. The overall appearance of FGFR2^{wt}-, FGFR2^{fusion}- and FGFR2^{EID}-expressing HB^C cell 3D cultures were strikingly different at low magnification (Fig. 8A). On zooming in, we found that unlike HB^B cells, the FGFR2^{fusion} impedes but does not block *de novo* lumen formation in HB^C cells (Fig. 8D). Instead of the large extended lumens exhibited by control and FGFR2^{wt}-expressing HB^C cells, FGFR2^{fusion}-expressing HB^C cells form many small, disorganized and often incomplete lumens (Fig. 1A; Fig. 8D,E; Supplemental Fig. 8A). Examination of the vertical z-plane revealed that while extended lumens in control and FGFR2^{wt}-expressing HB^C cells were centered and aligned, lumens in FGFR2^{fusion}-expressing HB^C cells were positioned randomly and often

remained intracellular, suggesting a lack of coordinated polarity (Fig. 8D,E; Supplemental Fig. 8A). Notably, FGFR2^{fusion}-expressing Caco2 cells exhibited a similar and striking lack of coordinated polarity, forming cysts containing multiple lumens (Supplemental Fig. 8B). In striking contrast, rather than lumens, the FGFR2^{EID} cells formed extended cords of cells that invaded the collagen/Matrigel ECM from the basal surface, explaining their strikingly different appearance at low magnification (Fig. 8A-E). Confocal images taken below the plane of the cell monolayer show that while FGFR2^{wt}-expressing cells formed a few short basal cords and FGFR2^{fusion}-expressing cells formed small spherical cell clusters, the FGFR2^{EID}-expressing cells formed an extended network of basally invasive cords (Fig. 8B,C). Basal cords did not extend from FGFR2^{EID}-expressing Caco2 cells suggesting that this consequence of FGFR2^{EID} expression is unique to mature lumen forming HB cells (Supplemental Fig. 8B). Importantly, as in HB^B cells (Supplemental Fig. 5A), neither mutant significantly drove cell proliferation in largely nondividing HB^C cells (Supplemental Fig. 8C). Thus, in addition to having different cell intrinsic effects, the two different FGFR mutants have markedly different impacts on biliary cell polarity and morphogenesis that could have profound impacts on tumor behavior.

Proliferation- and MAPK-independent phenotypic consequences of the FGFR2^{fusion} and FGFR2^{EID} in mature epithelial cells

Activation of FGFR triggers signaling through multiple pathways, but phosphorylation of the adaptor scaffold FRS and consequent MAPK pathway activation is thought to be responsible for the oncogenic consequences of mutant FGFR[17,33]. In HB^B cells, the FGFR2^{fusion} triggered strong tyrosine phosphorylation of FRS and activation of MAPK pathway effectors (SHP2, MEK), but the FGFR2^{EID} did not detectably activate any of them (Fig. 9A). This was surprising given that the same FGFR2^{EID} has been shown to activate FRS-MAPK signaling and transform NIH3T3 cells despite being immaturely glycosylated and ER-Golgi-trapped, which we verified (Fig. 6A,

Supplemental Figure 9A)[17,32]. However, the FGFR2^{EID} also did not activate FRS-MAPK signaling in HB^A cells or in mature lumen-competent HB^C cells where it was partially glycosylated and caused profound morphogenic consequences (Fig. 6A,B, Fig. 8, Fig. 9A). Also surprisingly, despite triggering strong FRS-MAPK signaling in NIH3T3, HB^A and HB^B cells, the FGFR2^{fusion} did so only modestly in HB^C cells where it also triggered strong morphogenic consequences (Fig. 9A). These observations suggest that signaling other than MAPK is playing an important role in the three-dimensional phenotypes elicited by the two mutants. Indeed, while FGFR inhibition completely rescued FGFR2^{fusion}- and FGFR2^{EID}-elicited 3D phenotypes, treatment with a MEK inhibitor (MEKi) only partially rescued both (Fig. 9B-E). It has recently been shown that activation of Src family tyrosine kinases (SFKs) is an important consequence of FGFR signaling in several developmental contexts[34]. Indeed, SFK activation in FGFR2^{fusion}-expressing HB^C cells and especially in FGFR2^{EID}-expressing HB^C cells was prominent relative to weak FRS-MAPK activation (Fig. 9F). The well-known role of SFKs in integrin-mediated cell-to-extracellular matrix (ECM) signaling suggests that they may be important drivers of the basal phenotypes driven by FGFR2^{EID} [35]. Consistent with this hypothesis, we found that in contrast to MEKi, pharmacologic SFK inhibition (SFKi) completely rescued the basal 'cords' elicited by FGFR2^{EID} in HB^C cells (Fig. 9G). It has been shown that MEKi relieves a key mechanism of negative feedback to FRS; indeed, immunoblotting revealed a reduction in size and increase in tyrosine phosphorylation of FRS in MEKi treated FGFR2^{fusion}- and FGFR2^{EID}-expressing HB^C cells as has been described in other cells (Fig. 9H)[36]. Interestingly, close inspection of the small cords that remain in MEKi-treated FGFR2^{EID}-expressing HB^C cells revealed the induction of small intercellular lumens that were not present in vehicle-treated FGFR2^{EID}-expressing cells (Fig. 9D). These observations are consistent with the possibility that FGFR2 signaling is compartmentalized in biliary epithelial cells, with FGFR2-FRS signaling important for apical surface generation and FGFR2-SFK signaling important basally, and that the balance of the two is important for creating a polarized epithelium during biliary morphogenesis. Our data suggest that the FGFR2^{fusion} and FGFR2^{EID}

may differentially deregulate these two compartments with profoundly different impacts on tumor progression and therapeutic response.

Discussion

Despite major advances in tissue engineering and cancer genomics, few studies actually focus on the interface between morphogenesis and tumorigenesis. Our studies underscore the facts that tumor-causing mutations often hijack features of morphogenesis in informative ways, and that physiologically relevant 3D models of morphogenesis can inform our understanding of tumor biology. Organogenesis-based models enable genetic and pharmacologic dissection of normal morphogenetic processes and more accurately model the earliest stages of tumorigenesis, the consequences of individual tumor-driving mutations, tumor progression and drug treatment response. Indeed, our studies have contributed substantially to our understanding of both biliary morphogenesis and tumorigenesis and the role of FGFR activity in both.

By establishing a panel of hepatoblast cell lines and deploying them in a quantitatively adapted physiological 3D model, we uncovered key steps in biliary morphogenesis that would not be captured by single-cell sequencing or other methods. For example, the discovery that lumen initiation and extension are separable events will allow us to study them individually. In particular, understanding how lumens extend and interconnect to form a functional biliary tubular network is essential to liver tissue engineering. Beyond physically maturing the apical surface by adding junctional components, cortical scaffolding, receptors and transporters (Fig. 2, Fig. 3, Supplemental Fig. 3C), lumen extension and interconnection requires the temporally and spatially appropriate remodeling of apical and junctional surface to enable coordinated alignment of new luminal surfaces among cells. For example, apical constriction is important for

limiting lumen extension in the developing liver and must normally occur perpendicular to the extending axis, perhaps due to planar polarized cues[9]. Successful lumen extension and interconnection likely also depends on the number and distribution of initiated lumens and spatially acquired planar polarity[37]. Lumen initiation occurs randomly across our 3D cultures (Fig. 1A, Supplemental Fig. 1D), and it is clear that in contrast to multipolar hepatocytes, developing biliary epithelial cells are strictly monopolar from the onset of polarization. So, for any cell, the initiation of a lumen in partnership with one neighboring cell precludes the initiation of another lumen with a different neighbor. If too many lumens are initiated, many rosettes form without extension (Supplemental Fig. 9B). This seems to be the case for MEKi-treated HB[C] cells, perhaps due to the release of feedback inhibition to FGFR, which increases lumen initiation, even within FGFR2[EID]-expressing basal cords (Fig. 9B,D). It is possible that lumen regression, which is thought to occur *in vivo*, can ease this restriction to facilitate lumen network formation[9]. A deeper appreciation of this dynamic process will be enabled by live-imaging in our 3D model.

The discovery that FGFR signaling is important for biliary *de novo* lumen formation is consistent with its known role in this process in other developmental contexts, and with the reported general requirement for FGFR in biliary morphogenesis in the chick[12,13,38]. Our studies of two different ICC-causing mutants yielded surprising new insights into the trafficking, signaling and cellular functions of FGFR. We found that the FGFR2[EID] is not fully glycosylated and can signal to FRS-MAPK from the ER-Golgi in NIH3T3 cells, as has been reported[32], but not in any of our HB cells or in AML-12 hepatocytes (Fig. 9A), suggesting that liver cells have mechanisms of silencing ER-Golgi-localized FGFR2. Identifying this mechanism will be important given that a significant proportion of FGFR2[wt] is also ER-Golgi-trapped in liver and other cell types and relief of this mechanism could be exploited by tumor cells (Supplemental Fig. 5G, Fig. 6A). Moreover, our studies reveal that glycosylation of the FGFR2[EID] and trafficking to the cell surface *does*

occur in more mature epithelial cells (Fig. 6A-B). These results suggest epithelial-specific regulation of both FGFR2 biosynthetic transport and membrane signaling, which could explain the lack of epithelial phenotypes or cancer predisposition in congenital craniosynostosis syndromes caused by inherited FGFR2 extracellular domain mutations, including Antley-Bixler and Pfeiffer syndromes, which can be caused by a FGFR2^{EID} mutation nearly identical to that used here (FGFR2^{W290C})[7,39].

Analysis of the FGFR2^{fusion} also uncovered key functional relationships between FGFR and epithelial biology. The observation that the FGFR2^{fusion} specifically disrupts E-cadherin-containing junctions by triggering a punctate peri-junctional appearance of E-cadherin is consistent with a role for FGFR in driving E-cadherin endocytosis[40] and could be an important mechanism of locally and dynamically removing E-cadherin-containing junctions to drive lumen initiation and extension. The enhanced surface availability of the FGFR2^{fusion} and widespread disruption of E-cadherin further suggests that FGFR2 activity is normally spatially restricted during *de novo* lumen formation, but that spatial restriction is compromised by the constitutive dimerization provided by the fusion partner and/or concomitant removal of the extreme FGFR2 C-terminal domain. Importantly, like the FGFR2^{EID}, signaling from the FGFR2^{fusion} to FRS-MAPK is dampened in mature epithelial cells, again suggesting that epithelial-specific mechanisms of dampening canonical FGFR2 signaling exist.

Our studies have important clinical implications, the most obvious of which is that the two FGFR2 mutants behaved differently by every criteria that we analyzed, suggesting that they elicit distinct tumor biologies. Therefore, FGFR^{fusion}- and FGFR2^{EID}-mutant tumors may exhibit distinct cooperating genetic events, pharmacologic vulnerabilities and resistance mechanisms, recruited microenvironments and progressive behaviors. Indeed, it has been noted that different FGFR mutations can differentially impact proliferation and drug sensitivity in fibroblasts[41]. Our

studies in a physiologically relevant cell type in uncovered additional proliferation-independent complexity and suggest that FGFR2[EID]-expressing tumors may be more invasive than FGFR2[fusion]-expressing tumors, which could help to explain why they have been reported to respond less readily to FGFRi in human patients[42,43]. It will be important to comparatively evaluate other types of FGFR2 mutations, such as transmembrane domain mutants and amplifications, that occur in ICC and to determine whether FGFR fusions and extracellular domain mutations that are common in other cancers yield similarly distinct biologies.

Importantly, although increased MAPK signaling is widely thought to be the tumor-driving consequence of FGFR mutation in ICC and other cancers, the proximal phenotypic consequences of both the FGFR[fusion]- and FGFR2[EID] in our models are largely proliferation- and MAPK-independent. This suggests that cooperating genetic events and/or microenvironment-provided signals unleash the full oncogenic potential of both mutants. Notably, the FGFR2[fusion] did not trigger proliferation even in HB[B] cells where it did induce FRS-MAPK signaling (Supplementary Fig. 5A). The release of strong negative feedback to FRS upon MEKi treatment also has important clinical implications as MEKi are being considered for ICC, either to enhance immunotherapy or target Ras or FGFR-mutant tumors[44]. Our studies suggest that MEKi could instead enhance noncanonical FGFR signaling, with unfortunate/unintended phenotypic consequences. Instead, the strong and distinct FRS-MAPK-independent consequences of both mutants underscore the importance of non-canonical FGFR signaling. Recent genetic studies in mice highlight the role of non-canonical FGFR signaling in skeletal morphogenesis and cell adhesion and point to Src as an important effector; it is therefore notable that some ICCs were found to be sensitive to pharmacologic Src inhibitors in a recent high-throughput *in vitro* screen[34,45]. Further studies that exploit the genetic and pharmacologic manipulability of this quantitative physiological 3D model will allow us to fully dissect the distinct mechanisms by which FGFR2[fusion] and FGFR2[EID] influence morphogenesis and tumorigenesis.

Materials and Methods

Cell culture

Single-cell-derived hepatoblast cell lines were generated from the livers of a litter of E14.5 mouse embryos as has been described[46,47]. This litter carried a homozygous unrecombined *Nf2^flox* allele that has no detectable phenotypic consequences[48]. They were then cultured on collagen-coated plates in growth medium containing DMEM/F-12, 10% FBS (Avantor), 1% penicillin-streptomycin (P/S), 50ng/mL EGF (Peprotech), 30ng/mL IGFII (Peprotech), and 10μg/mL Insulin (Sigma). NIH3T3 cells were obtained from ATCC and grown on uncoated plates in DMEM, 10% calf serum, 1% P/S. HEK293T and Caco2 cells (ATCC) were grown on uncoated plates in DMEM, 10% FBS, 1% P/S. AML12 cells (ATCC) were grown on uncoated plates in DMEM/F12, 10% FBS, 1% P/S, 1% Insulin/Transferrin/Selenium liquid supplement (Sigma), 40ng/μL dexamethasone (Sigma). All cells were cultured in a 37°C humidified incubator with 5% CO_2. For examining receptor distribution by IF, cells were plated on collagen-coated coverslips (Corning) and grown for 3 days at 37°C prior to fixation.

For 3D cell culture, we modified a previously described method[49]. Collagen gel was prepared by mixing 80% type I collagen (Corning) by volume with 10% 10X PBS and 10% 0.1N NaOH. This was then mixed with growth factor-reduced, phenol red-free Matrigel (Corning 356231) in an 80:20 collagen gel-to-Matrigel ratio. 150μL of gel was layered into each well of a prechilled 8-well chamber slide with clear borders (Ibidi) and the gels were incubated for 2 h (hours) at 37°C, to solidify them. Between $1x10^5$ and $4 x 10^5$ cells, as indicated in the figure legends, were suspended in 450μL of growth medium plus 5ng/mL HGF (Preprotech), added to each well and grown for 2 days with 5% CO_2 at 37°C. Medium was then removed and an additional 150 μL of gel of the same composition, followed by 300 μL of growth medium once the gels had been hardened for 2 h at 37°C, was layered on top. The cultures were incubated for an additional 3 days at 37°C prior to fixation. Due to the layout of 2 rows of 4 wells per slide, 3D experiments

were done as technical duplicates. For pHH3 quantifications, and where indicated in the figure legends, samples were cultured and fixed without the addition of the top layer of gel to facilitate antibody detection.

Pharmacological inhibitors

For 3D experiments, compounds were added one day prior to gel overlay unless indicated otherwise in the figure legends at the following concentrations: Infigratinib (Selleckchem; 3 µM), PD98509 (Selleckchem; 1 µM), and dasatinib (Selleckchem; 1 µM). For immunoblotting, cells were starved for 20 h in medium without FBS or added growth factors, then switched to medium containing inhibitors for 3 h before harvesting. For qPCR, cells were treated with 3µM BGJ398 for 16 h at steady state.

Plasmids

The pCL-ECO, pCMV-VSVG, pMSCV-FGFR2^wt, pMSCV-FGFR2-PHGDH and pMSCV-FGFR2-H167_N173 constructs were a generous gift from Nabeel Bardeesy[17,50]. The WI290>C substitution was generated in the pMSCV-FGFR2^wt construct using the Q5 site-directed mutagenesis kit (NEB). pMSCV-Blasticidin (empty vector) was a gift from David Mu (Addgene plasmid # 75085; http://n2t.net/addgene:75085 ; RRID:Addgene_75085). pUMVC was a gift from Robert Weinberg (Addgene plasmid #8449; http://n2t.net/addgene:8449 ; RRID:Addgene_8449).

Antibodies

The following antibodies were used: E-cadherin (1:500 for IF, 1:2000 for immunoblot; BD Biosciences, clone 36), β-catenin (1:250 for IF; Abcam clone E247), Ezrin (1:500 for IF; Invitrogen clone 3C-12), N-cadherin (1:500 for IF, 1:2000 for immunoblot; BD Biosciences clone 32), phospho Histone H3 (1:200 for IF; Cell Signaling Technology #9701), FGFR2 (1:200 for IF,

1:1000 for immunoblot; Cell Signaling Technology, clone D4H9), phospho-FRS2 Y196 (1:1000 for immunoblot; Cell Signaling Technology #3864), total FRS2 (1:500 for immunoblot; R&D Systems clone 462910), β-tubulin (1:2000 for immunoblot; Sigma clone B-7), phospho-SHP-2 (1:1000 for immunoblot; Cell Signaling Technology #3751), phospho-MEK (1:1000 for immunoblot; Cell Signaling Technology #9121), phospho-Src family (1:1000 for immunoblot; Cell Signaling Technology clone D49G4), gm130 (1:500 for IF; BD Biosciences, clone 35), ZO-1 (1:100, Invitrogen #61-7300). HRP-conjugated secondary anti-mouse and anti-rabbit antibodies were from Amersham. Alexa Fluor 488, 555, and 647-conjugated secondary antibodies were from ThermoFisher and used at 1:500.

Virus production and infection

Generation of MSCV retrovirus for infecting cells with FGFR2 constructs was achieved by PEI transfection of 1 μg pMSCV, 900 ng pCL-ECO (for mouse cells) or 900 ng pUMVC (for human cells) and 100 ng pCMV-VSVG per well of adherent HEK293T cells in a 6-well plate. Viral supernatants were collected at 2 and 3 days post-transfection. For infection, viral supernatants, containing 8 μg/mL polybrene, were added to cells grown to 30-50% confluence, then cells were selected and stable cell lines generated using blasticidin (Invivogen), at a concentration that had been experimentally determined to kill all uninfected cells after 7 days (12 μg/mL for HB^A; 6 μg/mL for HB^B; 7 μg/mL for HB^C; 5 μg/mL for 3T3; 10 μg/mL for Caco2; 12 μg/mL for AML12).

Immunofluorescence

For IF on cells grown in 3D, cells were fixed for 30 min (minutes) at 37° C with 3.7% formaldehyde in cytoskeletal buffer (10 mM MES Na$^+$ Salt, 138 mM KCl, 3 mM MgCl$_2$, 2 mM EGTA, pH 7.2). Samples were then incubated for 15 min at room temperature with 100 U/mL collagenase (Sigma), permeabilized for 30 min at 37° C with 0.5% Triton in PBS (with Ca^{++} and Mg^{++} ions), and then washed 3X for 15 min with 100 mM glycine in PBS. Cells were blocked for

1 h with 0.25% Triton in PBS, 0.1% BSA, 10% goat serum, then incubated overnight at 4°C with primary antibodies. This was followed by incubations with Alexa Fluor-conjugated secondary antibodies and conjugated Phalloidin (1:200; ThermoFisher). Nuclei were stained with DAPI and samples were mounted with Prolong Gold (ThermoFisher).

For IF of cells on coverslips, cells were fixed in 3.7% PFA in PBS (with Ca^{++} and Mg^{++}) for 15 min at room temperature, permeabilized with 0.2% Triton in PBS for 10 min, blocked for 30 min with 0.1% Triton in PBS, 0.1% BSA, 10% goat serum, and incubated overnight at 4°C with primary antibodies in blocking buffer. Cells were then incubated with Alexa Fluor-conjugated secondary antibodies, conjugated Phalloidin and DAPI.

Confocal images were captured with an LSM 710 or LSM 980 inverted laser-scanning confocal microscope (Carl Zeiss) using 20x, 40x (both water and oil-immersion) or 63x (oil-immersion) objectives. DAPI was excited with a 405-nm laser line of a diode laser. Alexa Fluor 488 and Alexa Fluor 555 probes were excited with the 488-nm or 514-nm laser line of an argon laser. Alexa Fluor 647 probes were excited with the 633-nm laser line of a helium-neo laser. Images were acquired as single images or z-stacks in sequential mode using ZEN Black software (2012; Carl Zeiss).

For HALO-mediated quantifications of lumens and dividing nuclei, samples were scanned in the AF488, AF647, and DAPI channels on a Vectra 3 whole slide scanning microscope (Akoya Biosciences), viewed using Phenochart software, and spectrally unmixed using InForm software.

qPCR

Total RNA was extracted from frozen cell pellets using TRIzol (Invitrogen), treated with DNase (NEB), then reverse transcribed with MMLV-RT (Promega) using oligo-dT primers. Fast Start

Universal SYBR Green Mix (Millipore Sigma) was used to amplify 0.5 µL of the RT reaction in a 15 µL total reaction volume. Triplicate samples were run on a Light Cycler 480 system (Roche) with cycling conditions of denaturation for 15 seconds at 95° C, annealing for 1 min at 60° C, and extension at 60° C, 45 cycles. Expression was normalized to GAPDH and fold-change computed using the $\Delta\Delta$Ct method.

Primer sequences are as follows. *Abcc2* forward 5′-AGCAGGTGTTCGTTGTGTGT-3′ and reverse 5′-CAGGAGGAATTGTGGCTTGTC-3′; *Cdhr5* forward 5′-TGCGCCAAAATTCTCCTTTGA-3′ and reverse 5′-AGGGATGACGGTTGTATTCACT-3′; *Cyp4f14* forward 5′-TGGCAACGGTTGATTTCAGAT-3′ and reverse 5′-TGCAGACTATCCAGAGTCATCAG-3′; *Epcam* forward 5′-GCGGCTCAGAGAGACTGTG-3′ and reverse 5′-CCAAGCATTTAGACGCCAGTTT-3′; *Gapdh* forward 5′-AGGTCGGTGTGAACGGATTTG-3′ and reverse 5′-TGTAGACCATGTAGTTGAGGTCA-3′; *Hnf1b* forward 5′-CCCAGCAATCTCAGAACCTC-3′ and reverse 5′-AGGCTGCTAGCCACACTGTT-3′; *Sox9* forward 5′-ACTCTGGGCAAGCTCTGGAG-3′ and reverse 5′-CGAAGGGTCTCTTCTCGCTCT-3′.

Western blotting

Cell pellets were lysed in mRIPA buffer with protease inhibitors (1% Triton X-100, 0.5% sodium deoxycholate, 0.1% SDS, 50 mM Tris-HCl at pH 7.4, 140 mM NaCl, 1 mM EDTA, 1 mM EGTA, 1 mM PMSF, 1 mM Na_3VO_4, 10 µg/mL leupeptin, 10 µg/mL pepstatin, 10 µg/mL aprotinin), for 1 h on ice, then lysates cleared by centrifugation. 40 µg of protein were loaded on SDS-PAGE gels, transferred to PVDF membranes, and incubated at 4° C overnight with antibodies diluted in 5% milk or 5% BSA (for phospho-specific antibodies). The membranes were then incubated with secondary antibodies, exposed to ECL substrate and film-developed.

Enzymatic deglycosylation assay

To determine the glycosylation state, the cell lysates were treated with endoglycosidase H (Endo H, New England Biolabs, P0702) or Peptide-N-Glycosidase F (PNGase F, New England Biolabs, P0704) as per manufacturer instructions. Briefly, the combination of 50 µg lysates and glycoprotein denaturing buffer was incubated at 100° C for 10 min. The denatured proteins were then treated with 2,000 U Endo H or 1,250 U PNGase F at 37°C for 1 h and analyzed by immunoblot.

Cell surface biotinylation

Cells were seeded in 6-well plates, grown to confluence and then placed on ice for 10 min before rinsing 3X with ice-cold PBS containing Ca^{2+} and Mg^{2+}. Biotinylation was performed by incubating the cells with 0.5 mg/mL EZ-Link Sulfo-NHS-SS-Biotin (ThermoFisher Scientific, 21335) in cold PBS at 4° C for 30 min with gentle swirling every 5 min to ensure even coating. After incubation, cells were rinsed 2X with cold PBS and washed 2X with cold 50 mM NH_4Cl in PBS to quench unbound biotin. Cells were then lysed in CSK buffer (50 mM NaCl, 10 mM PIPES pH 6.8, 3 mM $MgCl_2$, 300 mM sucrose, 1% Triton-X 100, 10 mM NaF, 10 mM NaP_2O_7, 1X protease inhibitors) for 1 h on ice. Lysates were cleared by centrifugation at 14,000 x g for 30 min, and supernatants were incubated with streptavidin beads (ThermoFisher Scientific, 53117) for 2 h at 4° C with rotation. The beads were then washed 4X with CSK buffer, and biotinylated proteins eluted with 2x sample buffer containing β-mercaptoethanol at 95° C. Eluates and whole cell lysates as the input were analyzed by immunoblot.

Image analysis and statistics

ImageJ software (version 2.14, National Institutes of Health) was used for all image processing and analysis. The displayed images were produced from single confocal slices or projections of z-stack images. Background was removed with rolling ball background subtraction. Lookup

tables were applied to produce final images. x-z or y-z images were generated by re-slicing z-stack images. Junction height was quantified by measuring the length of a straight line drawn along E-cadherin labeled cell boundaries in x-z or y-z views of z-stack images. The junctional intensity of E-cadherin, N-cadherin or F-actin was determined by plotting the intensity profile of a line (10 µm in length) drawn perpendicular to the center of a cell-cell junction. The ratio of junctional to non-junctional intensity was calculated by dividing the average intensity of the middle of the line (~3-7 µm) by the average intensity of the ends of the line (~ 0-3 µm; 7-10 µm). Cord area was quantified by creating a binary threshold mask to define cords and measuring the percentage area covered by cords per field. Lumen polarity was measured in x-z views of z-stack images by drawing rectangles around the lumen perimeter as defined by F-actin staining and determining the Z coordinates of the center of the lumen relative to the center of a rectangle drawn around the full height of the cell monolayer. The absolute value of the difference between these values was graphed to represent the polarity of lumens relative to the monolayer. After acquisition of whole-slide scans of 3D cultures, the spectrally unmixed images were imported into HALO[TM] (Version 3.5) and fused. Annotation layers were selected to determine lumen and nuclear parameters within selected regions of the samples, typically the interior of the gel versus the exterior. Cell recognition and nuclear segmentation was trained and optimized using HiPlex FL module (Indica Labs), using both the DAPI and autofluorescence channels in at least five regions within each annotation. pHH3+ nuclei were counted in the AF647 channel, and the ratio of pHH3+ to total nuclei used as a measure of cell division. For lumen measurements, a supervised machine learning algorithm (Random Forest classifier) was trained on at least three randomly selected regions in the AF488 Phalloidin channel, to recognize lumens of differing sizes and shapes and to distinguish them from junctional Phalloidin. Data was output as number of lumens, lumen area, and lumen perimeter. For determining a lumen circularity index, the following formula was used: Circularity = $(4\pi*Area)/(Perimeter^2)$. Data from all analyses were

imported into Prism 10 for plotting graphs and performing statistical analyses. The statistical tests used to compare groups are indicated in the figure legends.

RNA sequencing sample preparation

Total RNA was extracted from frozen cell pellets using TRIzol reagent (Invitrogen, 15596018) according to the manufacturer's protocol. Residual DNA was removed by treatment with DNase I (New England Biolabs, M0303). The concentration of the extracted RNA was quantified using the Ribogreen fluorescence-based assay (Life Technologies, R11490) with a Victor X2 fluorometer (PerkinElmer). The integrity of the RNA was assessed using an Agilent Technologies 2100 Bioanalyzer, with samples achieving an RNA Integrity Number (RIN) value of 7.0 or higher considered suitable for further processing.

RNAseq analysis

Libraries were prepared using the TruSeq Stranded mRNA LT Sample Prep Kit (Illumina) and sequenced on an Illumina NovaSeq6000 S4 v1.5 sequencer by Psomagen, which also provided processed quantification for each transcript as counts. RNAseqQC[51] was used to assess library complexity, number of reads and genes detected, replicate variability and for hierarchical clustering of samples. Testing for differential gene expression between conditions was performed using DESeq2 (PMID: 25516281, v1.38.3). clusterProfiler (PMID: 34557778, v4.6.2) was used to perform gene set enrichment analysis (GSEA) with the Hallmark MSigDB genesets (PMID: 2677102, v7) and Gene Ontology over-representation analysis was done using the Cellular Components gene sets (PMID: 10802651, PMID: 36866529, 2022-07-01). All computational analyses were performed using custom scripts (available upon request) in R-4.2.2.

Acknowledgments

Competing interests. The authors declare no competing interests.

References:

1. Buckley, C.E. & St Johnston, D. Apical-basal polarity and the control of epithelial form and function. *Nat Rev Mol Cell Biol* **23**, 559-577 (2022).
2. Whitford, M.K.M. & McCaffrey, L. Polarity in breast development and cancer. *Curr Top Dev Biol* **154**, 245-283 (2023).
3. Peglion, F. & Etienne-Manneville, S. Cell polarity changes in cancer initiation and progression. *J Cell Biol* **223**(2024).
4. Almagro, J., Messal, H.A., Elosegui-Artola, A., van Rheenen, J. & Behrens, A. Tissue architecture in tumor initiation and progression. *Trends Cancer* **8**, 494-505 (2022).
5. Du, Z. & Lovly, C.M. Mechanisms of receptor tyrosine kinase activation in cancer. *Mol Cancer* **17**, 58 (2018).
6. Clark, J.F. & Soriano, P.M. Pulling back the curtain: The hidden functions of receptor tyrosine kinases in development. *Curr Top Dev Biol* **149**, 123-152 (2022).
7. McDonell, L.M., Kernohan, K.D., Boycott, K.M. & Sawyer, S.L. Receptor tyrosine kinase mutations in developmental syndromes and cancer: two sides of the same coin. *Hum Mol Genet* **24**, R60-66 (2015).
8. Lemaigre, F.P. Development of the Intrahepatic and Extrahepatic Biliary Tract: A Framework for Understanding Congenital Diseases. *Annu Rev Pathol* **15**, 1-22 (2020).
9. Benhamouche-Trouillet, S*., et al.* Proliferation-independent role of NF2 (merlin) in limiting biliary morphogenesis. *Development* **145**(2018).
10. Tanimizu, N*., et al.* Intrahepatic bile ducts are developed through formation of homogeneous continuous luminal network and its dynamic rearrangement in mice. *Hepatology* **64**, 175-188 (2016).
11. Sigurbjornsdottir, S., Mathew, R. & Leptin, M. Molecular mechanisms of de novo lumen formation. *Nat Rev Mol Cell Biol* **15**, 665-676 (2014).
12. Durdu, S*., et al.* Luminal signalling links cell communication to tissue architecture during organogenesis. *Nature* **515**, 120-124 (2014).
13. Ryan, A.Q., Chan, C.J., Graner, F. & Hiiragi, T. Lumen Expansion Facilitates Epiblast-Primitive Endoderm Fate Specification during Mouse Blastocyst Formation. *Dev Cell* **51**, 684-697 e684 (2019).
14. Fabris, L*., et al.* Pathobiology of inherited biliary diseases: a roadmap to understand acquired liver diseases. *Nat Rev Gastroenterol Hepatol* **16**, 497-511 (2019).
15. Ilyas, S.I*., et al.* Cholangiocarcinoma - novel biological insights and therapeutic strategies. *Nat Rev Clin Oncol* **20**, 470-486 (2023).
16. Vogel, A., Segatto, O., Stenzinger, A. & Saborowski, A. FGFR2 Inhibition in Cholangiocarcinoma. *Annu Rev Med* **74**, 293-306 (2023).
17. Cleary, J.M*., et al.* FGFR2 Extracellular Domain In-Frame Deletions Are Therapeutically Targetable Genomic Alterations That Function as Oncogenic Drivers in Cholangiocarcinoma. *Cancer Discov* **11**, 2488-2505 (2021).
18. Arai, Y*., et al.* Fibroblast growth factor receptor 2 tyrosine kinase fusions define a unique molecular subtype of cholangiocarcinoma. *Hepatology* **59**, 1427-1434 (2014).
19. Wu, Y.M*., et al.* Identification of targetable FGFR gene fusions in diverse cancers. *Cancer Discov* **3**, 636-647 (2013).
20. De Moerlooze, L*., et al.* An important role for the IIIb isoform of fibroblast growth factor receptor 2 (FGFR2) in mesenchymal-epithelial signalling during mouse organogenesis. *Development* **127**, 483-492 (2000).
21. Chitnis, A.B., Nogare, D.D. & Matsuda, M. Building the posterior lateral line system in zebrafish. *Dev Neurobiol* **72**, 234-255 (2012).

22. Antoniou, A., *et al.* Intrahepatic bile ducts develop according to a new mode of tubulogenesis regulated by the transcription factor SOX9. *Gastroenterology* **136**, 2325-2333 (2009).

23. Zong, Y., *et al.* Notch signaling controls liver development by regulating biliary differentiation. *Development* **136**, 1727-1739 (2009).

24. Loeuillard, E., Fischbach, S.R., Gores, G.J. & Ilyas, S.I. Animal models of cholangiocarcinoma. *Biochim Biophys Acta Mol Basis Dis* **1865**, 982-992 (2019).

25. Kendre, G., *et al.* The Co-mutational Spectrum Determines the Therapeutic Response in Murine FGFR2 Fusion-Driven Cholangiocarcinoma. *Hepatology* **74**, 1357-1370 (2021).

26. Sampaziotis, F., *et al.* Cholangiocyte organoids can repair bile ducts after transplantation in the human liver. *Science* **371**, 839-846 (2021).

27. Babboni, S., *et al.* Cholangiocyte Organoids: The New Frontier in Regenerative Medicine for the Study and Treatment of Cholangiopathies. *J Clin Med* **13**(2024).

28. Broutier, L., *et al.* Human primary liver cancer-derived organoid cultures for disease modeling and drug screening. *Nat Med* **23**, 1424-1435 (2017).

29. Lidsky, M.E., *et al.* Leveraging patient derived models of FGFR2 fusion positive intrahepatic cholangiocarcinoma to identify synergistic therapies. *NPJ Precis Oncol* **6**, 75 (2022).

30. Tanimizu, N., Miyajima, A. & Mostov, K.E. Liver progenitor cells develop cholangiocyte-type epithelial polarity in three-dimensional culture. *Mol Biol Cell* **18**, 1472-1479 (2007).

31. Valle, J.W., Lamarca, A., Goyal, L., Barriuso, J. & Zhu, A.X. New Horizons for Precision Medicine in Biliary Tract Cancers. *Cancer Discov* **7**, 943-962 (2017).

32. Tanizaki, J., *et al.* Identification of Oncogenic and Drug-Sensitizing Mutations in the Extracellular Domain of FGFR2. *Cancer Res* **75**, 3139-3146 (2015).

33. Wu, Q., *et al.* EGFR Inhibition Potentiates FGFR Inhibitor Therapy and Overcomes Resistance in FGFR2 Fusion-Positive Cholangiocarcinoma. *Cancer Discov* **12**, 1378-1395 (2022).

34. Clark, J.F. & Soriano, P. Diverse Fgfr1 signaling pathways and endocytic trafficking regulate mesoderm development. *Genes Dev* **38**, 393-414 (2024).

35. Mitra, S.K. & Schlaepfer, D.D. Integrin-regulated FAK-Src signaling in normal and cancer cells. *Curr Opin Cell Biol* **18**, 516-523 (2006).

36. Lax, I., *et al.* The docking protein FRS2alpha controls a MAP kinase-mediated negative feedback mechanism for signaling by FGF receptors. *Mol Cell* **10**, 709-719 (2002).

37. Raab, M., *et al.* Van Gogh-like 2 is essential for the architectural patterning of the mammalian biliary tree. *J Hepatol* **81**, 108-119 (2024).

38. Yanai, M., *et al.* FGF signaling segregates biliary cell-lineage from chick hepatoblasts cooperatively with BMP4 and ECM components in vitro. *Dev Dyn* **237**, 1268-1283 (2008).

39. Azoury, S.C., Reddy, S., Shukla, V. & Deng, C.X. Fibroblast Growth Factor Receptor 2 (FGFR2) Mutation Related Syndromic Craniosynostosis. *Int J Biol Sci* **13**, 1479-1488 (2017).

40. Bryant, D.M., Wylie, F.G. & Stow, J.L. Regulation of endocytosis, nuclear translocation, and signaling of fibroblast growth factor receptor 1 by E-cadherin. *Mol Biol Cell* **16**, 14-23 (2005).

41. Nakamura, I.T., *et al.* Comprehensive functional evaluation of variants of fibroblast growth factor receptor genes in cancer. *NPJ Precis Oncol* **5**, 66 (2021).

42. Chae, Y.K., *et al.* Phase II Study of AZD4547 in Patients With Tumors Harboring Aberrations in the FGFR Pathway: Results From the NCI-MATCH Trial (EAY131) Subprotocol W. *J Clin Oncol* **38**, 2407-2417 (2020).

43. Nogova, L., *et al.* Evaluation of BGJ398, a Fibroblast Growth Factor Receptor 1-3 Kinase Inhibitor, in Patients With Advanced Solid Tumors Harboring Genetic Alterations

in Fibroblast Growth Factor Receptors: Results of a Global Phase I, Dose-Escalation and Dose-Expansion Study. *J Clin Oncol* **35**, 157-165 (2017).

44. Ruggieri, A.N.*, et al.* Combined MEK/PD-L1 Inhibition Alters Peripheral Cytokines and Lymphocyte Populations Correlating with Improved Clinical Outcomes in Advanced Biliary Tract Cancer. *Clin Cancer Res* **28**, 4336-4345 (2022).
45. Saha, S.K.*, et al.* Isocitrate Dehydrogenase Mutations Confer Dasatinib Hypersensitivity and SRC Dependence in Intrahepatic Cholangiocarcinoma. *Cancer Discov* **6**, 727-739 (2016).
46. Curto, M., Cole, B.K., Lallemand, D., Liu, C.H. & McClatchey, A.I. Contact-dependent inhibition of EGFR signaling by Nf2/Merlin. *J Cell Biol* **177**, 893-903 (2007).
47. Strick-Marchand, H. & Weiss, M.C. Embryonic liver cells and permanent lines as models for hepatocyte and bile duct cell differentiation. *Mech Dev* **120**, 89-98 (2003).
48. Giovannini, M.*, et al.* Conditional biallelic Nf2 mutation in the mouse promotes manifestations of human neurofibromatosis type 2. *Genes Dev* **14**, 1617-1630 (2000).
49. Tanimizu, N., Miyajima, A. & Mostov, K.E. Liver progenitor cells fold up a cell monolayer into a double-layered structure during tubular morphogenesis. *Mol Biol Cell* **20**, 2486-2494 (2009).
50. Goyal, L.*, et al.* TAS-120 Overcomes Resistance to ATP-Competitive FGFR Inhibitors in Patients with FGFR2 Fusion-Positive Intrahepatic Cholangiocarcinoma. *Cancer Discov* **9**, 1064-1079 (2019).
51. F, Z. R package (2024).

Figure Legends

Figure 1. Quantitative imaging of a panel of hepatoblast cell lines that capture discrete stages of lumen competence in a physiological 3D model. A. Confocal images (top) and HALO-based callout (bottom) of lumens formed by HB of each class. B. High resolution confocal images of individual lumens formed by HB^B cells and stained with phalloidin (F-actin, white; top) and E-cadherin (green; top, middle) and Ezrin (magenta) and β-catenin (green; bottom). C. HALO-based quantitation of lumen abundance (lumens/cell; left), size (lumen area; middle) and extension (lumen circularity; right). Bars represent the SEM +/- mean. P values were calculated using a one-way ANOVA with Tukey's multiple comparisons test (lumen abundance, *p<0.05; ***p<0.001, ns = not significant) or Mann-Whitney test (lumen area and circularity, ***p<0.001). For lumen abundance, each datapoint represents the scan of an entire 3D culture chamber with 0 (HB^A), 25,981 (HB^B) or 7,231 (HB^C) lumens. For lumen area and circularity each datapoint represents an individual lumen. Scale bars = 20 µm.

Figure 2. Progressive junction maturation accompanies the ability to form immature and mature lumens. A. Immunoblot showing E-cadherin and N-Cadherin levels across our panel of HBs, NIH3T3, Caco2 and AML12 cells. B. Confocal images depicting F-actin (white), E-cadherin (green), N-cadherin (magenta) and ZO-1 (cyan) localization to cell-cell junctions in HB^A, HB^B and HB^C cells that were cultured without the top layer of gel. C. Vertical *x-z* and *y-z* views depict junction height in HB^A, HB^B and HB^C cells. D. Quantitation of junction height from C. P values were calculated using a one-way ANOVA with Tukey's multiple comparison's test (***p<0.001). Scale bars = 10 µm.

Figure 3. RNAseq reveals that the acquisition of lumen competence is accompanied by increased apical gene expression. A. Heatmap showing hierarchical clustering-based

RNAseq profiles of representative HB cell lines of each class of lumen competence. Grouped columns reflect RNAseq profiles of three *independent passages* of each cell line as opposed to technical replicates. B. Top Gene Ontology (GO) Cellular Components that are upregulated in mature lumen competent (HB^C) versus lumen incompetent (HB^A) HB cells. C. Validation of the progressive increase of selected apical gene mRNAs with lumen competence by qPCR. Bars represent the mean +/- SEM. P values were calculated using a one-way ANOVA with multiple comparisons test ($*p<0.05$; $**p<0.01$; $***p<0.001$). D. Two-sided bar plots showing the top Hallmark genesets that are upregulated in association with lumen initiation (left) or lumen extension (right). E. Venn diagram depicting minimal overlap in genes of the GO geneset 'Apical part of the cell' (GO:0045177) that are upregulated with early stage (no lumens to immature lumens; magenta) and late stage (immature lumens to mature extended lumens; cyan) lumen phenotypes.

Figure 4. FGFR promotes *de novo* lumen formation and biliary morphogenesis. A. Confocal images of HB^B cells in 3D cultures grown without and with the FGFRi infigratinib and stained with phalloidin (F-actin; white) and DAPI (blue). Scale bars = 20 µm. B. HALO-mediated quantitation of lumen abundance in control and FGFRi-treated cultures. Bars represent mean +/- SEM. P values were calculated using a Mann-Whitney test ($***p<0.001$). C. Measurement of apical gene expression in control and FGFRi-treated HB^B cells by qPCR. Bars represent mean +/- SEM. P values were calculated with an unpaired two-tailed Student's t-test ($*p<0.1,**p<0.01,***p<0.001$). D. Bar plots depicting the top GO Cellular Components that are upregulated by FGFR2^{wt} expression in HB^B cells. E. Venn diagram depicting the number of apical genes whose expression is upregulated by HBs in association with early (magenta) or late (cyan) stages of lumen competence versus those promoted by FGFR2^{wt} overexpression (gray).

Figure 5. Distinct localizations and phenotypic consequences of FGFR2^{fusion} and FGFR2^{EID} in HB^B cells. A. Graphic of the two mutant FGFR2 isoforms with the locations of the fused segment and extracellular domain mutations in red. B. Confocal images depicting lumen formation (F-actin, white) in HB^B cells expressing FGFR2^{wt}, FGFR2^{EID}, FGFR2^{fusion} and FGFR2^{fusion} plus FGFRi. Scale bar = 20 µm. C. Quantitation of lumen abundance across the entire 3D chambers from (B) plus at least one biological replicate. Bar represents mean +/- SEM. P values were calculated using a one-way ANOVA with Tukey's multiple comparisons test (***$p<0.001$). D. Confocal images depicting E-cadherin based junctions (green) in HB^B cells expressing FGFR2^{wt}, FGFR2^{EID}, FGFR2^{fusion} and FGFR2^{fusion} plus FGFRi. Scale bar = 10 µm. E. Quantitation of junctional integrity in 3D cultures of HB^{B}s expressing FGFR2^{wt}, FGFR2^{EID} and FGFR2^{fusion} with and without FGFRi. P values were calculated using a one-way ANOVA with multiple comparisons test (***$p<0.001$). F. Venn diagram depicting overlapping numbers of genes upregulated by FGFR2^{wt}, FGFR2^{EID} and FGFR2^{fusion} in HB^B cells. G. *Top*, Immunoblot of lysates from FGFR2^{wt}-, FGFR2^{EID}- and FGFR2^{fusion}-expressing HB^B cells treated with EndoH (E) or PNGase (P). M = mature, I = immature, U = unglycosylated. *Bottom*, Pie chart representation of the proportion of immature and mature glycosylated forms of each version of FGFR2. H. Immunoblot of total and surface biotinylated proteins from FGFR2^{wt}, FGFR2^{fusion} and FGFR2^{EID}-expressing cells.

Figure 6. Trafficking of and signaling from FGFR2^{EID} depends on epithelial character. A. *Top*, immunoblots of lysates from NIH3T3 fibroblasts, HB^A, HB^B and HB^C HBs and Caco2 epithelial cells treated with EndoH (E) or PNGase (P). M = mature, I = immature, U = unglycosylated. * = irrelevant human-specific background band. *Bottom*, Pie charts representing the proportions of immature (gray) and mature (black) glycosylated forms of each version of FGFR2. B. Immunoblot showing input and surface biotinylated FGFR2^{wt}, FGFR2^{fusion} and FGFR2^{EID} levels in HB^C cells.

Figure 7. Junction-disrupting activity of FGFR2^{fusion} depends on epithelial character. A. Confocal images depicting the distribution of junctional E-cadherin (top, green) and F-actin (bottom, white) in HB^A, HB^B and HB^C cells expressing FGFR2^{wt} (top) or FGFR2^{fusion} (bottom). B. Quantitation of junctional E-cadherin measured as the ratio of junctional to non-junctional intensity in FGFR2^{wt} and FGFR2^{fusion}-expressing HB^A (left), HB^B (middle) and HB^C (right) cells. P values were calculated using a one-way ANOVA with Tukey's multiple comparisons test (*$p<0.2$, ***$p<0.001$). C. High resolution confocal images depicting junctional F-actin (white) and E-cadherin (green) in FGFR2^{fusion}-epressing HB^C cells. D. Confocal images depicting the distribution of N-cadherin (magenta) in FGFR2^{wt}- and FGFR2^{fusion}-expressing HB^B cells that were cultured without the top layer of gel. E. Quantitation of junctional N-cadherin (magenta) in FGFR2^{wt}- and FGFR2^{fusion}-expressing HB^B cells. Each datapoint represents the ratiometric measurement across a single boundary between two cells (see Methods). Scale bars = 10 µm.

Figure 8. Differential impact of FGFR2^{EID} and FGFR2^{fusion} on lumen formation and morphogenesis in mature lumen-competent HB^C cells. A. Low power immunofluorescence images of the entire 3D culture of FGFR2^{wt}-, FGFR2^{fusion}- and FGFR2^{EID}-expressing HB^C cells stained for F-actin (green). Scale bar = 20 µm. B. Confocal images of a z-plane basal to the cell monolayer in FGFR2^{wt}-, FGFR2^{fusion}- and FGFR2^{EID}-expressing HB^C cells stained for F-actin (magenta) and DAPI (blue). Scale bar = 50 µm. C. Quantitation of the area of cords in FGFR2^{wt}-, FGFR2^{fusion}-, and FGFR2^{EID}-expressing HB^C cells. P values were calculated with one-way ANOVA with Tukey's multiple comparisons test (***$p<0.001$). D. *Top*, x-y and *bottom*, x-z confocal images of F-actin (magenta), E-cadherin (green) and DAPI (blue) stained 3D cultures of FGFR2^{wt}-, FGFR2^{fusion}- and FGFR2^{EID}-expressing HB^C cells. Dashed line depicts the basal cord emerging from the cell monolayer in FGFR2^{EID}-expressing HB^C cells. Scale bars = 10 µm. E. Quantitation of lumen alignment in FGFR2^{wt}-, FGFR2^{fusion}- and FGFR2^{EID}-expressing HB^C

cells. P values were calculated using a one-way ANOVA with Tukey's multiple comparisons t-test (***p<0.001).

Figure 9. MAPK-independent signaling contributes to FGFR2 mutant 3D phenotypes in mature epithelial cells. A. Immunoblots showing FGFR2^{wt}-, FGFR2^{fusion}- and FGFR2^{EID}-induced signaling in HB^A, HB^B and HB^C cells. B. *Top,* x-y, and *bottom,* x-z confocal images of F-actin (magenta), E-cadherin (green) and DAPI (blue) stained 3D cultures of HB^C cells expressing FGFR2^{fusion} treated with vehicle (DMSO), FGFRi (2μM) or MEKi (1μM). Scale bars = 10 μm. C. Quantitation of lumen abundance and alignment in FGFRi- and MEKi-treated FGFR2^{fusion}-expressing HB^C cells. D. *Left,* Confocal images at z planes below the cell monolayer of FGFR2^{EID}-expressing HB^C cells treated with vehicle (DMSO), FGFRi, or MEKi. *Right*, high resolution confocal images of individual cell cords in vehicle- or MEKi-treated FGFR2^{EID}-expressing HB^C cells. Scale bars = 50 μm. E. Quantitation of cord area in D. F. Immunoblot showing pSFK levels in FGFR2$^{fusion}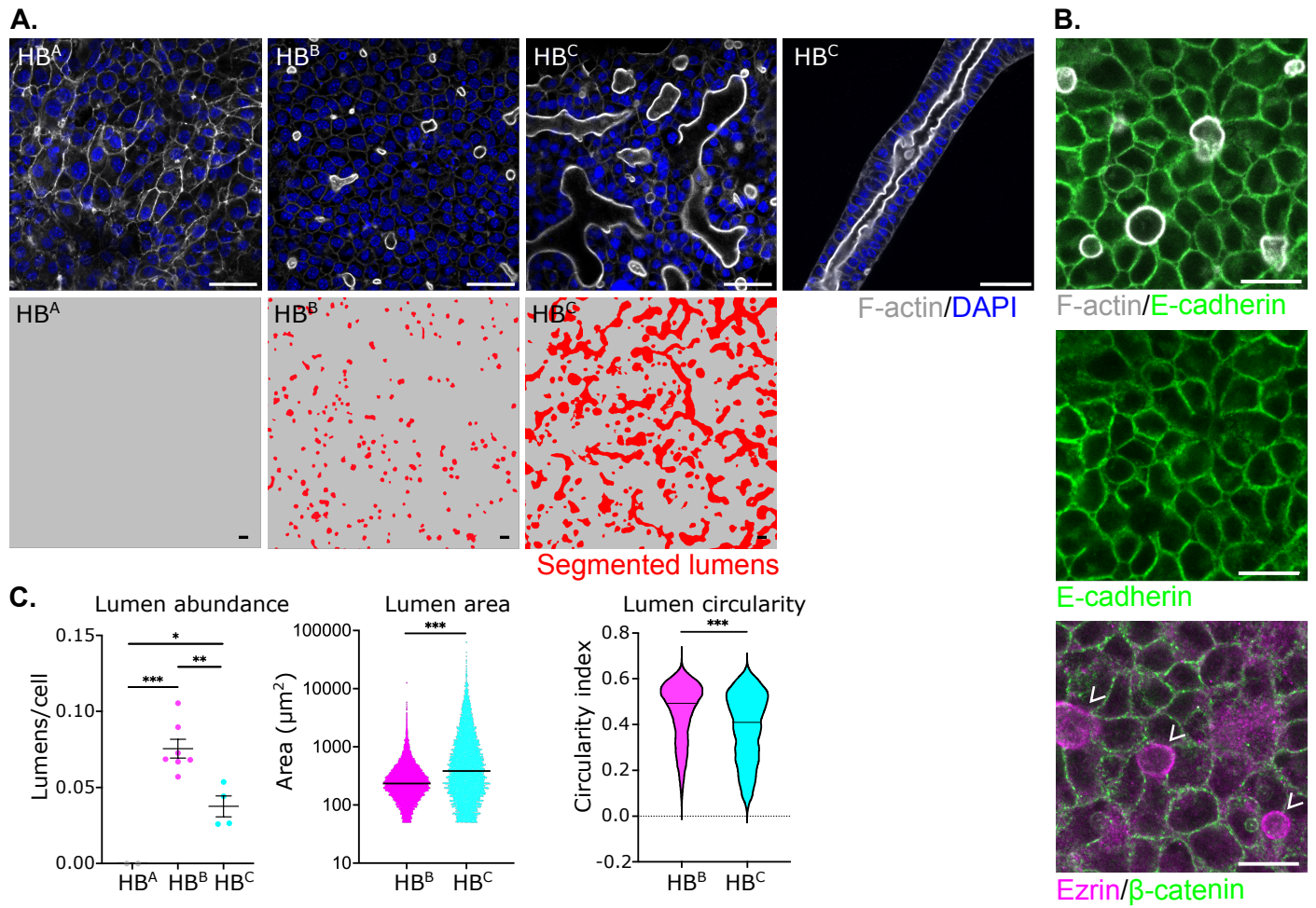$ and FGFR2^{EID}-expressing HB^C cells with and without SFKi treatment. St = starved, SS = steady state. G. Quantitation of cord area in vehicle (DMSO) and SFKi-treated (dasatinib;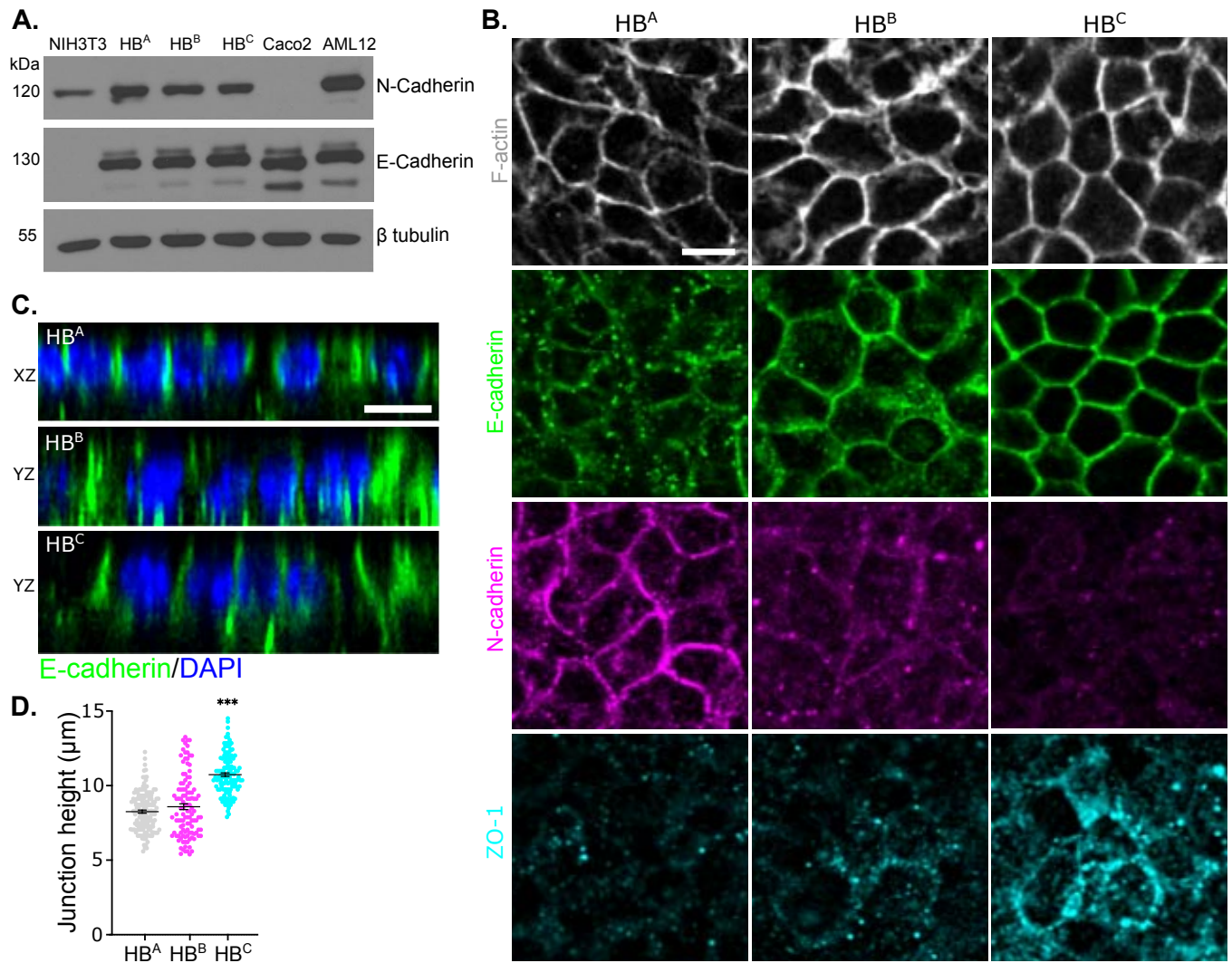 1μM) FGFR2-EID-expressing HBC cells. H. Immunoblots showing pFRS size and levels in vehicle- and MEKi-treated FGFR2^{fusion}- and FGFR2^{EID}-expressing HB^C cells.

O'Loughlin, Zhang, Chiasson-MacKenzie et al. Figure 1

A.

B.

C.

Lumen abundance

Lumen area

Lumen circularity

Segmented lumens

F-actin/DAPI

F-actin/E-cadherin

E-cadherin

Ezrin/β-catenin

O'Loughlin, Zhang, Chiasson-MacKenzie et al. Figure 2

O'Loughlin, Zhang, Chiasson-MacKenzie et al. Figure 3

A. HB^B / +FGFRi — F-actin/DAPI

B. Lumens/Cell; HB^B vs HB^B+FGFRi (***)

C. Cdhr5 (*), Cyp4f14 (***), Epcam (**) — Fold Change, Control vs FGFRi

D. Upregulated GO Cellular Components (Count): apical part of cell, apical plasma membrane, collagen-containing extracellular matrix, secretory granule, basal part of the cell, receptor complex, basal plasma membrane, synaptic membrane, basolateral membrane, cell projection membrane

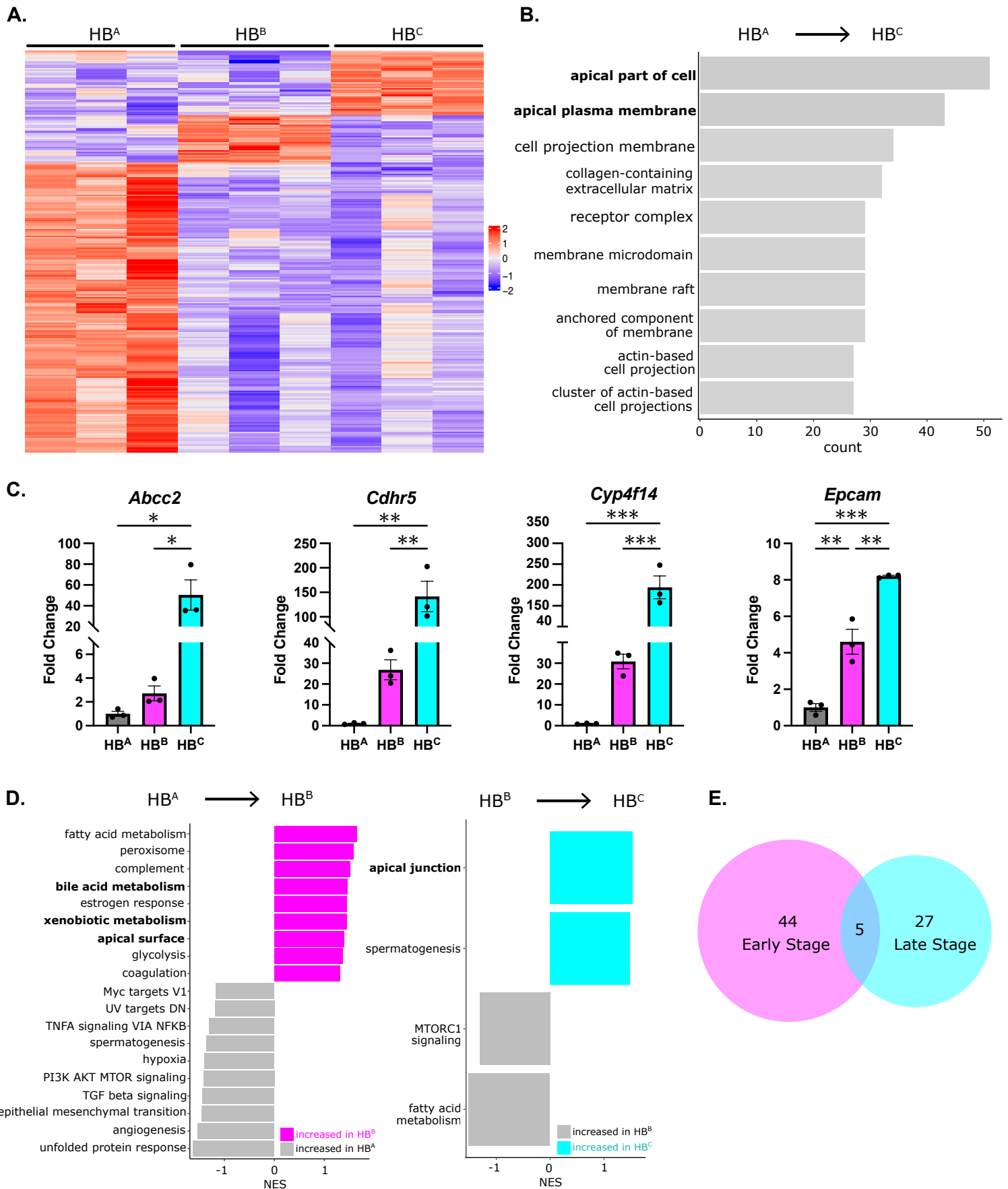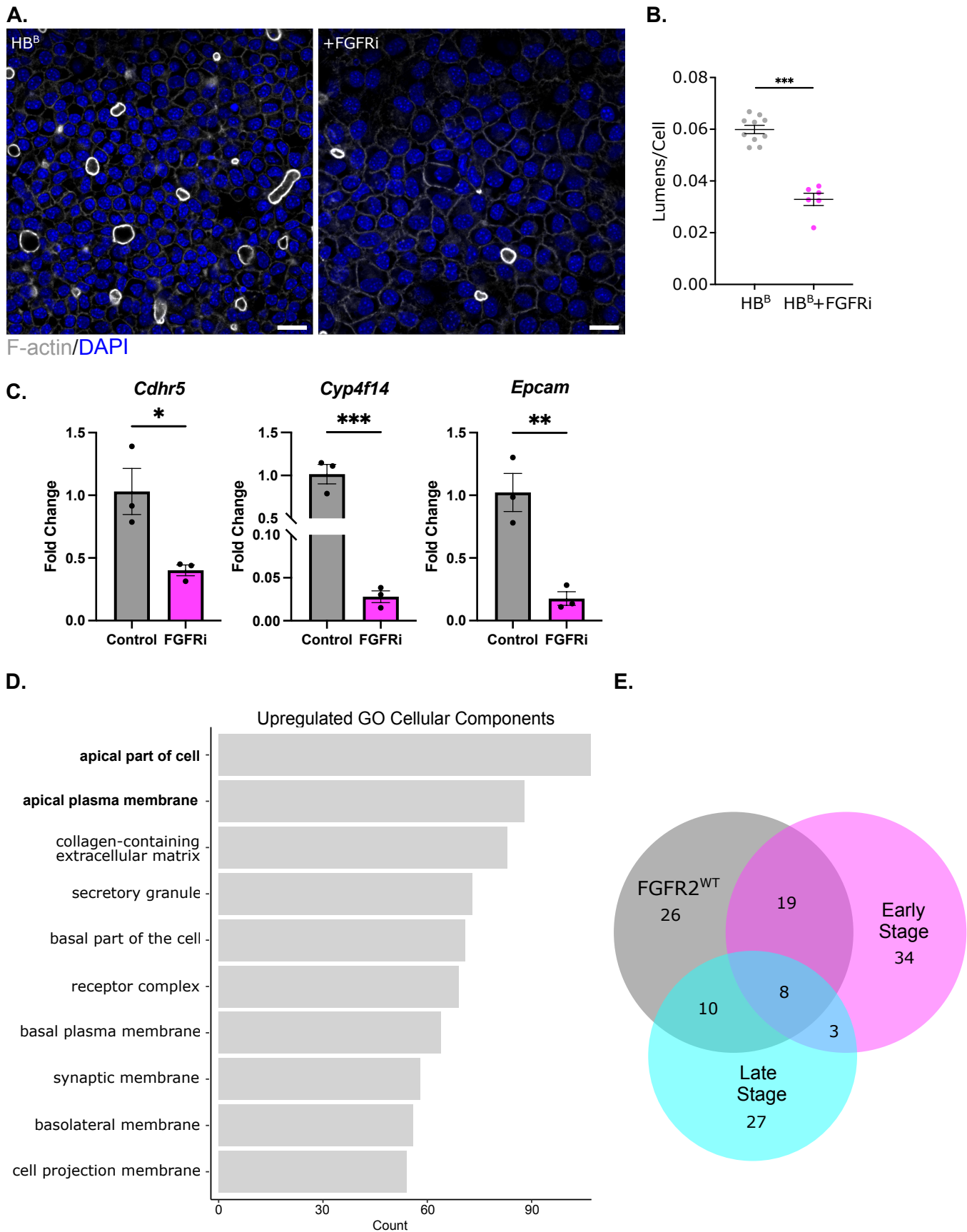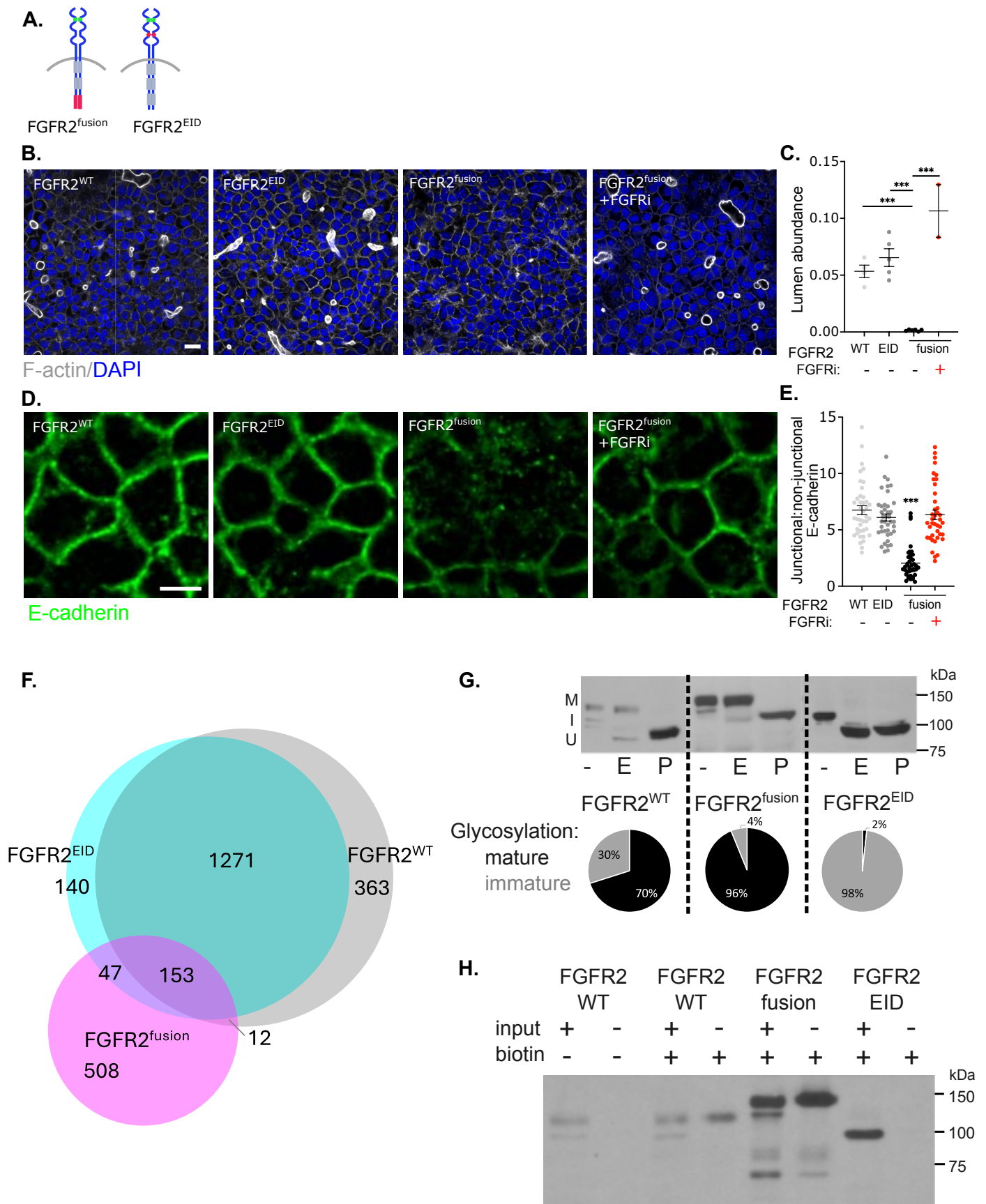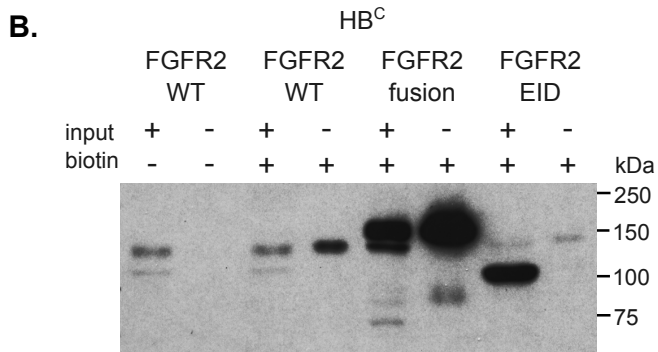**E.** FGFR2^{WT} 26, Early Stage 34, Late Stage 27; 19, 10, 8, 3
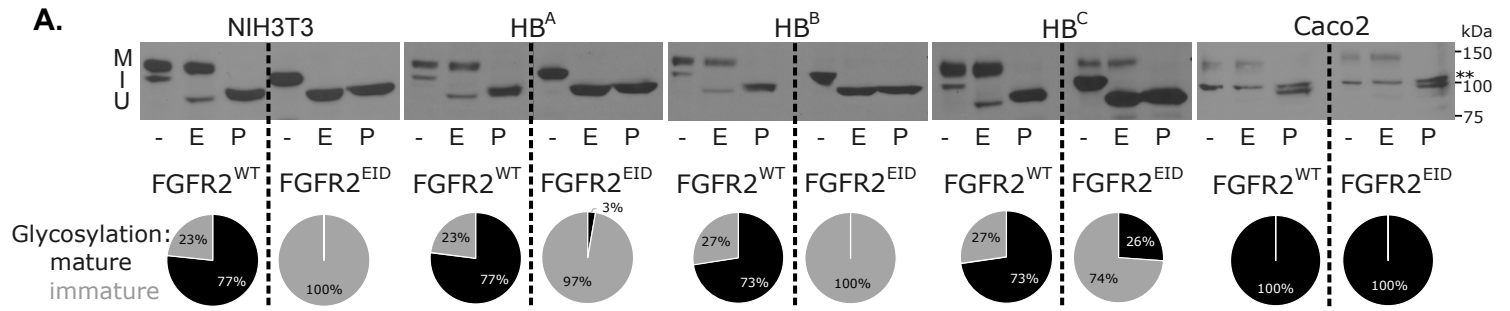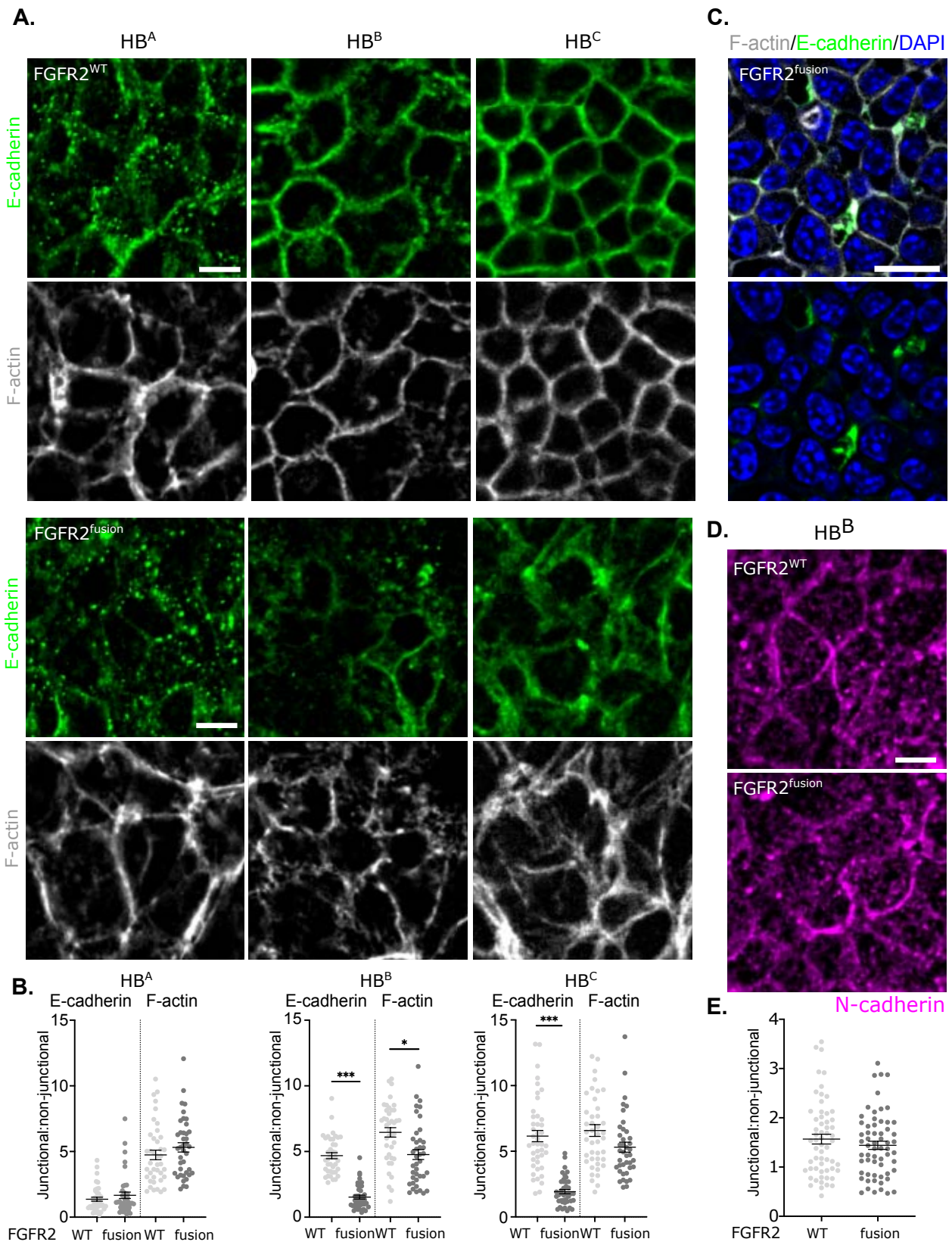
O'Loughlin, Zhang, Chiasson-MacKenzie et al. Figure 5

O'Loughlin, Zhang, Chiasson-MacKenzie et al. Figure 6

O'Loughlin, Zhang, Chiasson-MacKenzie et al. Figure 7

O'Loughlin, Zhang, Chiasson-MacKenzie et al. Figure 8

O'Loughlin, Zhang, Chiasson-MacKenzie et al. Figure 9

A. Western blots for FGFR2, pFRS, FRS, pMEK, and pSHP2 across FGFR2^{wt}, FGFR2^{fusion}, and FGFR2^{EID} for HB^A, HB^B, HB^C.

B. FGFR2^{fusion} Vehicle, +FGFRi, +MEKi — F-actin/E-cadherin/DAPI

C. Lumen polarity — Veh. FGFRi MEKi, FGFR2^{fusion}

D. FGFR2^{EID} Vehicle, +FGFRi, +MEKi; Vehicle, +MEKi — F-actin/DAPI

E. % Cord Area — Veh. FGFRi MEKi, FGFR2^{EID}

F. FGFR2^{fusion}, FGFR2^{EID}: FGFR2, pSFK; SS, St, SFKi 200nM, SFKi 1μM, SS, St, SFKi 200nM, SFKi 1μM

G. % Cord Area — Veh., SFKi

H. FGFR2^{fusion}, FGFR2^{EID}: pFRS, FRS; SS, St, MEKi 1μM, SS, St, MEKi 1μM